



**HAL**  
open science

## Consolidated Chemical Provinces on Mars

A. Rani, A. Basu Sarbadhikari, D. Hood, O. Gasnault, S. Nambiar, S.  
Karunatillake

► **To cite this version:**

A. Rani, A. Basu Sarbadhikari, D. Hood, O. Gasnault, S. Nambiar, et al.. Consolidated Chemical Provinces on Mars. *Geophysical Research Letters*, 2022, 49 (14), pp.e2022GL099235. 10.1029/2022GL099235 . hal-03840877

**HAL Id: hal-03840877**

**<https://hal.science/hal-03840877v1>**

Submitted on 6 Nov 2022

**HAL** is a multi-disciplinary open access archive for the deposit and dissemination of scientific research documents, whether they are published or not. The documents may come from teaching and research institutions in France or abroad, or from public or private research centers.

L'archive ouverte pluridisciplinaire **HAL**, est destinée au dépôt et à la diffusion de documents scientifiques de niveau recherche, publiés ou non, émanant des établissements d'enseignement et de recherche français ou étrangers, des laboratoires publics ou privés.



30 **Abstract**

31 Chemical provinces were defined on Mars a decade ago using orbital nuclear  
32 spectroscopy of K, Th, Fe, Si, Ca, Cl, and H<sub>2</sub>O. However, past multivariate analyses yielded  
33 three sets of provinces, suggesting methodologic variability. Province-stability to the  
34 inclusion of Al and S is also unknown, presenting additional uncertainties for geologic  
35 insight. Here we consolidate key multivariate methods to define the first cross-validated  
36 provinces. In southern highlands, the highly incompatible K and Th show non-uniform  
37 distribution with higher values in mid Noachian and Hesperian than late Noachian – early  
38 Hesperian volcanic terrains. Silica- and Al-depletion trends from Noachian to Amazonian  
39 indicate highly differentiated mantle with variable degree of melting. Late Hesperian  
40 lowlands are highly depleted in Al and enriched in K and Th, consistent with volcanic  
41 resurfacing from a low-degree partially melted, garnet-rich mantle. Furthermore, older  
42 volatile-rich regions such as Medusae Fossae Formation exhibit igneous geochemistry,  
43 consistent with water-limited isochemical weathering throughout Mars's history.

44

45 **Plain Language Summary**

46 Topographically Mars can be divided into two large regions: southern highlands and  
47 northern lowlands. However, the compositional evolution of these two landforms and their  
48 source characteristics remains unclear. Therefore, using enhanced satellite nuclear  
49 spectroscopic data, we develop a set of consolidated geochemical provinces of Mars using  
50 three multivariate analysis techniques. We identified the correlation of distinct geochemical  
51 provinces with mapped geologic units, which demonstrates the effect of bedrock composition  
52 over bulk soil composition. Our study depicts discrete igneous provinces within the southern  
53 highlands, which follow a secular chemical pattern, indicating a highly differentiated mantle

54 source with an evolving formation pressure and degree of melting. The northern lowlands, on  
55 the other hand, are uncorrelated with the chemical trend of southern highland provinces,  
56 suggesting a distinct evolution. Our findings further reveal that regardless of volatile  
57 enrichment, igneous crustal composition dominates over chemical alteration signatures  
58 indicating a limited role of liquid water on the martian landscape.

59

## 60 **1. Introduction**

61 *A trilogy* of multivariate cluster analysis methods applied to the chemical maps  
62 derived from Mars Odyssey gamma-ray and neutron spectroscopy (GRS) initially identified  
63 chemical provinces and supported interpretations of regional-scale geology ([Karunatillake et al., 2009](#);  
64 [Gasnault et al., 2010](#); [Taylor et al., 2010](#)). However, the lack of an inter-  
65 methodological synthesis to characterize geological processes has hindered subsequent works  
66 and stymied advances with other datasets (cf., [Rogers & Hamilton 2015](#)). Furthermore, key  
67 chemical maps used in subsequent papers ([Baratoux et al., 2014](#); [Ojha et al., 2018](#); [Plesa et al., 2018](#))  
68 were unavailable or only in a preliminary state for the original trilogy: Aluminium  
69 (Al), sensitive to both igneous evolution and secondary mineralogy (cf., [Nimmo & Tanaka, 2005](#);  
70 [Ehlmann et al., 2011](#); [McLennan, 2012](#)); and Sulfur (S), sensitive to cycling processes  
71 within the martian critical zone across the atmosphere and crust ([Halevy et al., 2007](#); [King & McLennan, 2010](#)).

73 Here we use nine elemental mass fraction maps from the GRS: key rock-forming  
74 elements (Fe, Si, Ca, and Al) with large ion lithophiles (K and Th) and volatiles  
75 (stoichiometrically equivalent H<sub>2</sub>O, Cl, and S) to resolve the aforementioned challenges. We  
76 synthesize and advance prior multivariate methods ([Karunatillake et al., 2009](#); [Gasnault et al., 2010](#);  
77 [Taylor et al., 2010](#)) to derive the first consolidated chemical provinces of Mars. We

78 consider three of the provinces as case studies on geologic insight, revealing diverse mantle  
79 sources and magmatic processes in volcanic areas, characterizing possible global ashfall  
80 units, and evaluating the relative roles of igneous versus aqueous environments.

81

## 82 **2. Data and Methods**

83 We use chemical maps derived from GRS spectra to delineate the chemically distinct  
84 provinces. The average decimetre sampling depth and coarse spatial resolution of GRS  
85 overcome the effects of fine dust mantles making GRS elemental analysis ideal for primary  
86 and secondary geological process studies on broad scales. GRS measures the energy  
87 spectrum of gamma photons emitted from the martian surface and characteristic spectral  
88 peaks allow us to measure the abundance and distribution of most major rock-forming  
89 elements, along with some minor elements present on the martian surface. There are two  
90 main processes on the martian surface that give rise to gamma-photon emission. Gamma  
91 photons can be emitted from the decay of natural radioactive elements (K and Th) or  
92 emissions induced by cosmic particle interactions with the martian atmosphere and non-  
93 radioactive elements of the martian surface. However, due to increasing H (reported as  
94 stoichiometric H<sub>2</sub>O mass fractions) towards the poles causing mass dilution for radioactive  
95 elements and compositional modelling issues for others due to neutron moderation, derived  
96 chemical maps are restricted to the mid-to-low latitudes, roughly within  $\pm 50^\circ$ . Furthermore,  
97 chemical maps are generated at a resolution of  $5^\circ \times 5^\circ$  due to broad footprint of the GRS  
98 instrument (Boynton et al., 2007). We use the latest refined datasets of GRS, including Al  
99 and S used in the literature (cf., Hood et al., 2016, 2019; Ojha et al., 2018, 2021), and  
100 compare them with GRS data used a decade ago (Boynton et al., 2007; Karunatillake et al.,  
101 2009; Gasnault et al., 2010; Taylor et al., 2010), including the archived data at the NASA

102 Planetary Database System (<https://pds-geosciences.wustl.edu/ody/ody-m-grs-5-elements>  
103 [v1/odgm\\_xxxx/data/smoothed/](#)). The delineation of provinces also mitigates the substantial  
104 spatial autocorrelation inherent in the GRS data by associating large chemical deviations with  
105 multi-pixel regions rather which are larger than the GRS instrument footprint ([Karunatillake](#)  
106 [et al., 2009](#)). The detailed description and comparison of old versus latest refined datasets of  
107 GRS are described in Supplementary Information S1.

108

## 109 **2.1. Multivariate Cluster Analysis**

110 We apply three multivariate cluster analyses to discern a set of internally uniform  
111 chemical provinces that reflect the compositional variability of the martian crust. The three  
112 methods (**Supporting Information S1.2** provides more details) consist of non-hierarchical  
113 clustering with principal component analysis (NHC-PCA: [Taylor et al., 2010](#)), hierarchical  
114 clustering with principal component analysis (HC-PCA: [Gasnault et al., 2010](#)), and modified  
115 student's t-test to distinguish spatially overlapping Gaussian tail clusters (t-GTC:  
116 [Karunatillake et al., 2009](#)).

117 The three methods optimize clustering differently but still present spatially  
118 overlapping trends suggestive of distinct provinces. NHC-PCA optimizes Euclidian distances  
119 between cluster centers, where the number of clusters is specified a priori. In comparison,  
120 HC-PCA builds a hierarchy of clusters using a top-down clustering approach based on a  
121 divisive algorithm ([Kaufman & Rousseeuw, 2005](#)), where the complete martian landscape  
122 mapped by GRS belongs to one cluster and is split iteratively, moving down the hierarchy to  
123 highlight the differences between the sub-clusters. The modified t-GTC method identifies  
124 spatially contiguous areas where two or more elements deviate from their respective average  
125 mid-to-low latitude crustal abundances by one standard deviation or greater. The t-GTCs and

126 HC-PCA-derived provinces reduce spatial autocorrelation biases by using unclassified  
127 (boundary) pixels to separate provinces from each other. Complementarily, the NHC-PCA  
128 method delineates border-sharing provinces.

129 We combine the intermediate provinces from the NHC-PCA, HC-PCA, and t-GTC  
130 methods into a consolidated map using a spatial contouring approach. A contour map of  
131 provinces is made by categorizing the regions into three levels: provinces derived from all  
132 three-methods overlapping, provinces with any two-methods overlapping, and provinces with  
133 no overlap (**Figure S1**). We demarcate the boundaries of final provinces resulting from at  
134 least two-methods overlapping, reducing the spatial uncertainty in any method (**Supporting**  
135 **Information S2** provides more details). Provinces that deviate minimally from the average  
136 martian crust (AMC) composition (**Supporting Information S2.1** and **S2.2**) are omitted so  
137 that the consolidated chemical province map highlights crustally distinct regions. In addition,  
138 we use mapped geology ([Tanaka et al., 2014](#)) for context on chemical trends.

139

### 140 **3. Results**

141 All three methods lead to large chemically uniform provinces, with minimal intra-  
142 province compositional variance, reinforcing the subdued variability in chemical maps of  
143 Mars. The intermediate chemical province sets resulting from the three underlying methods  
144 (**Supporting Information S2** provides more details) are labeled numerically (Province-1 to  
145 Province-6; **Figures 1a-c** and **Tables S1** and **S2**). Province-2 from NHC-PCA and HC-PCA  
146 methods lacks the minimum criterion of at least two methods overlapping (**Figure S1**;  
147 **Supporting Information S2** provides more details), and Province-4 is compositionally  
148 identical to the AMC within statistical uncertainty. Therefore, Province-2 and 4 are de-  
149 prioritized in the consolidated chemical province map (**Figure 1d**). Moreover, provinces that

150 overlap spatially across the methods are compositionally similar even if driven by different  
151 multivariate methods (**Tables S2, S3**). This further justifies our contour-consolidation method  
152 yielding the merged chemical province map (**Figure 1** and **Tables 1** and **S3**). Overall,  
153 overlapping areas labeled as ‘Province-1’ in **Figures 1a-c** have been combined into  
154 ‘Province-A’, ‘Province-3’ into ‘Province-B’, ‘Province-5’ into ‘Province-C’, and ‘Province-  
155 6’ into ‘Province-D’, resulting in four consolidated provinces (**Figure 1d** and **Tables 1** and  
156 **S1**). Compositional consistency across the numeric intermediate provinces enables this  
157 synthesis (**Supporting Information S2**). While geographically widely separated areas may  
158 constitute a single province, such regions show some compositional heterogeneity.

159

### 160 **3.1. Distinct Geochemical Provinces**

161 Four geographically distributed regions in the southern highlands constitute Province-  
162 A (**Figure 1d**). This province broadly represents mid and late Noachian highlands (> 30%) to  
163 early Hesperian aged volcanic units (> 20%) (**Figures 2a** and **S2**), containing many of the  
164 large Hesperian volcanic provinces. This province is enriched in Al and depleted in K, Th,  
165 and volatiles (H<sub>2</sub>O, S, Cl) relative to the AMC (**Figure 2b** and **Tables 1, S3, and S4**;  
166 **Supporting Information S2.2**). The K/Th and S/Cl ratios are above average, while the Fe/Si  
167 ratio is consistent with the AMC.

168 Province-B comprises Amazonian and Amazonian-Hesperian aged volcanic units (>  
169 30%) with Amazonian to Hesperian transitional geological units (~ 18%) (**Figures 2a** and  
170 **S2**). The distribution of K and Th is consistent with the AMC ([Taylor et al., 2006](#)); however,  
171 the K/Th ratio is slightly low compared to the AMC (**Figure 2b** and **Tables 1, S3** and **S4**;  
172 **Supporting Information S2.2**). This province is moderately depleted in Si, Ca, and Fe and  
173 highly depleted in Al, while the volatiles (especially Cl and S) are highly enriched relative to



174 the AMC. The S/Cl ratio is depleted from preferential Cl enrichment. Compared to the AMC,  
175 the Fe/Si ratio is below average.

176 Province-C consists of two geographic regions: Sinus Meridiani (SM) and the  
177 Medusae Fossae Formation (MFF), dominated by mid-Noachian highlands (~ 40 %) (**Figures**  
178 **1d, 2a, and S2** and **Table S1**). These regions are enriched in volatiles (H<sub>2</sub>O, Cl, and S) (cf.  
179 [Diez et al. 2008](#); [Feldman et al., 2011](#); [Maurice et al., 2011](#)), while Fe, Ca are slightly  
180 enriched relative to the AMC (**Figure 2b** and **Tables 1, S3 and S4; Supporting Information**  
181 **S2.2**). The ratio of S/Cl and K/Th is consistent with the AMC. However, Fe enrichments  
182 make the Fe/Si ratio higher relative to the AMC.

183 Two regions of broadly late Hesperian lowlands form Province-D (> 60%) (**Figures**  
184 **2a and S2**). It is confined to Southern Acidalia Planitia and Utopia Planitia of the Northern  
185 lowland near the dichotomy boundary (**Figure 1d** and **Table S1**). Since both these regions  
186 are found within the northern lowlands and the northern extent of each is obscured by the  
187 chemical mapping boundary (**Supporting Information S1**), they may constitute a larger,  
188 contiguous region. The broader extent of Province-D, which includes the western and eastern  
189 part of this province, spatially overlaps with the TES-derived Surface Type 2 mineralogy in  
190 the martian northern lowlands ([Bandfield et al., 2000](#); [Rogers et al., 2007](#); [Rogers &](#)  
191 [Hamilton 2015](#)). This province is highly depleted in Al, enriched in Si, Fe, K, and Th relative  
192 to the AMC (**Figure 2b** and **Tables 1, S3 and S4**), contrasting with other provinces. The  
193 K/Th and S/Cl ratio is consistent with the AMC, whereas Fe/Si is higher.

194

## 195 **4. Discussion**

### 196 **4.1. Extent of aqueous alteration and K/Th trends**

197 We first evaluate the extent of aqueous alteration evident at regional scales to  
198 decimeter depths. The Chemical Index of Alteration  
199 ( $CIA = Al_2O_3 / (Al_2O_3 + CaO + Na_2O + K_2O) \times 100$ ) in standard molar abundances of oxides  
200 corresponding to the provinces A-D is  $< 50$ , which indicates no signature of weathering  
201 (**Figure 2c**) at these broad scales. The K/Th ratio is similar across all the provinces, and with  
202 the AMC within statistical uncertainty (**Figure 2b**). Specifically, K/Th ratio is effectively  
203 invariant with the abundance of the volatiles ( $H_2O$ ,  $SO_3$ , and Cl) even across the maximum in  
204 Province-C to a minimum in Province-A (**Figure 3a**). The most incompatible mapped  
205 elements, K and Th (partition coefficient  $\ll 1$ ; [Borg & Draper, 2003](#)) do not fractionate in the  
206 solid phases during magmatic processes. Collectively, our study shows that even the volatile-  
207 rich regions are compositionally consistent with water-limited isochemical weathering  
208 throughout Mars's geologic history ([Hurowitz & McLennan, 2007](#); [Tosca et al., 2008](#)).  
209 Consequently, the provinces are broadly representative of well-preserved igneous processes  
210 at least to decimeter depth scales and averaged over a few hundred kilometres horizontally.

211

## 212 4.2. Secular chemical trends on Mars

213 Earlier work by [Taylor et al. \(2010\)](#) grouped all volcanic landscapes into a single  
214 province irrespective of age. However, our study supports the findings ([Karunatillake et al.,](#)  
215 [2009](#); [Gasnault et al., 2010](#)) that volcanic regions form separate provinces by age (**Figure**  
216 **2a**), as shown by [Baratoux et al. \(2011\)](#). Moreover, the minimally weathered secular volcanic  
217 composition of provinces A-C in the southern highlands of Mars shows distinct geochemical  
218 trends. Unlike southern highlands, Province-D, the late Hesperian lowland unit, deviates from  
219 the secular chemical trend (**Figure 3b-d**), indicating distinct lithology. The provinces A-C  
220 from mid-Noachian to Amazonian show Al-, Fe-, Si- and Ca-depletion (**Figure 3b-d**). As

221 hypothesized by [Balta & McSween \(2013\)](#), higher SiO<sub>2</sub> in older regions of Mars may indicate  
222 dehydration melting of the mantle with hundreds of mg/kg water, similar to that of Province-  
223 A and -C of our study, in contrast to the relatively silica-depleted younger Province-B. Unlike  
224 Earth, considering a stagnant-lid regime of Mars ([Golombek & Phillips, 2009](#); [Grott et al.,](#)  
225 [2013](#)), the decrease of SiO<sub>2</sub> and concomitant increase in olivine component in the parent  
226 magma from the oldest to youngest volcanic terrains of southern highlands could be  
227 explained by the growth of lithospheric thickness, which would increase the formation  
228 pressure, supporting the results of [Baratoux et al. \(2013\)](#). This contrasts with the topmost  
229 micron-layer observation by Thermal Emission Spectrometer (TES), suggestive of  
230 weathering reflected by the non-detection of olivine in the Hesperian highland terrains, at the  
231 spatial resolution of 1 pixel per degree ([Rogers & Hamilton, 2015](#)). GRS-scale footprints in  
232 this study consistently reveal the igneous crustal composition albeit weathering processes was  
233 prevalent during martian surface evolution. In addition, high Ca/Al for Province-B and -D  
234 could indicate a path for sampling a high-pressure, garnet-rich source ([Treiman, 2005](#);  
235 [Dasgupta & Hirschmann, 2007](#); [Balta & McSween, 2013](#)). The abundances of K and Th are  
236 relatively low in late Noachian – early Hesperian Province-A as compared to Hesperian-  
237 Amazonian Province-B and mid-Noachian Province-C in the highland volcanic terrains  
238 (**Figure 3e**). Earlier studies advocated the early Noachian crust building phenomenon for the  
239 enrichment of these large ion lithophile elements (LILEs: K and Th) in Noachian than  
240 Hesperian terrains ([Rogers & Hamilton, 2015](#)). However, our study shows that the youngest  
241 volcanic province also contains a high relative abundance of those LILEs, which contradicts  
242 the hypothesis of LILE fractionation during the early Noachian crust formation. Moreover,  
243 the non-systematic trend of the abundances of LILEs and other secular chemical trends may  
244 necessitate complex melting processes in a highly differentiated mantle source on a regional

245 to global scale (cf. [Basu Sarbadhikari et al., 2016; 2017; Udry et al., 2020](#)) that existed from  
246 the early-stage evolution of Mars.

247 Compared to prior works, the emergence of distinct regions as well as the exclusion  
248 of previously suggested provinces (**Figure 1d**) reflects our methodological advances along  
249 with the use of Al and S. Given the collective distinctness among the consolidated chemical  
250 provinces, we consider three regions for detailed case studies: Lunae Planum, Medusae  
251 Fossae Formation, and Southern Acidalia Planitia (**Figure 1d**).

252

### 253 **4.3. Lunae Planum (LP) in Province-A**

254 LP region is a geologically distinct plateau of early Hesperian-aged highland material  
255 ([Tanaka et al., 2014](#)), which lies between Chryse Planitia and Olympus Mons in Province-A  
256 (**Figure 1d**). Geochemically, the LP is depleted in K, Th, and H<sub>2</sub>O relative to the AMC. LP  
257 follows the general K and Th crustal correlation on Mars and substantially overlaps with the  
258 K and Th distribution in Hesperia and Thaumasia Planum (**Figures 3e and S3**).  
259 Consequently, LP's K and Th depletion likely reflects volcanic resurfacing, not aqueous  
260 weathering ([Taylor et al., 2006](#)). H<sub>2</sub>O depletion in the LP is also comparable in magnitude to  
261 that in the vicinity of Greater Thaumasia ([Hood et al., 2016](#)). Given minimal chemical  
262 weathering across the provinces (Section 4.1), the H<sub>2</sub>O depletion is likely volcanic and could  
263 suggest a dry mantle source as predicted for Hesperian volcanism (cf., [Balta & McSween,](#)  
264 [2013](#)). However, that mantle evolution model also predicts high Th abundances, not seen in  
265 our study. Overall, the LP likely follows the same volcanic evolution trends as identified in  
266 the Greater Thaumasia area, i.e., low H<sub>2</sub>O abundance and temporally decreasing K and Th,  
267 maybe a part of the same evolving volcanic province ([Hood et al., 2016](#)). Furthermore, higher

268 K and Th abundance within LP relative to Greater Thaumasia could place it as the oldest  
269 member of an underlying volcanic series.

270

#### 271 **4.4. Medusae Fossae Formation (MFF) in Province-C**

272 The discrete wind-sculpted outcrops of the mid-Noachian MFF extend along the  
273 martian equator (**Figure 1d**) and their origin remains uncertain (c.f., [Kerber & Head, 2010](#);  
274 [Zimbelman & Scheidt, 2012](#); [Wilson et al., 2018](#)). Geochemically, the MFF region is highly  
275 enriched in Fe, Ca, and volatiles (SO<sub>3</sub>, Cl, and H<sub>2</sub>O) relative to the AMC (**Figure S4**) ([Keller  
276 et al., 2006](#)). However, the abundance of K, Th, Al, Si, and the value of K/Th is consistent  
277 with the martian crust. As highly incompatible elements in igneous processes, the ratio of  
278 Cl/K would inherit the initial mantle abundance ([Taylor et al., 2010](#)). Although the ratio is  
279 globally maintained, the MFF region shows significantly different Cl/K than the rest of Mars.  
280 Chlorine is highly abundant, and K is generally lower than that in AMC (**Figures 3e and S4**),  
281 consistent with Cl enrichment in airborne dust and volcanic aerosol in the MFF ([Newsom &  
282 Hagerty, 1997](#); [Goetz et al., 2005](#)). Meanwhile, high S and Cl content, moderately high H<sub>2</sub>O  
283 (**Figure S5**), fine-grained nature, preserved primary mineralogy, and extensive erosional  
284 features suggest that MFF is the source of the global dust reservoirs of Mars ([Ojha et al.,  
285 2018](#)). Thus, our work supports the provenance of martian dust from mostly mechanical  
286 weathering and transport of a pyroclastic ashfall unit, which possibly arose from SW-oriented  
287 paleo-winds during Tharsis volcanic eruptions ([Keller et al., 2006](#); [Diez et al., 2009](#)). Our  
288 results don't support the hypothesis of water-ice existence in polar layer-like deposits to  
289 explain the volatile enrichment in the equatorial MFF ([Wilson et al., 2018](#)). Summarily, the  
290 voluminous pyroclasts of MFF are most likely the product of low-moderate degree partial

291 melting of a distinct volatile-rich mantle source during mid-Noachian age in comparison to  
292 the late Noachian - Amazonian volcanic provinces of the martian highlands.

293

#### 294 **4.5. Southern Acidalia Planitia (SAP) in Province-D**

295 SAP is a late Hesperian plain area (Tanaka et al., 2014) in the northern lowlands that  
296 geographically lies between Tharsis and Arabia Terra and is part of Province-D (Figure 1d).  
297 Geochemically, SAP is enriched in K, Th, Fe, Si and depleted in Al relative to the rest of the  
298 AMC (Figure S6). Despite K and Th enrichment, the K/Th ratio of SAP is consistent with  
299 the martian crust (Figures 3e and S6), which suggests primary rock composition  
300 (Karunatillake et al., 2006; Taylor et al., 2006), diverging from the extensive alteration  
301 posited by Bouley et al. (2020). Al/Si versus Mg/Si plots of SAP (Figure S7a) show a slope  
302 different from the martian crust but resembling that of younger martian meteorites (after,  
303 McSween et al., 2009). The Al depletion in SAP best correlates with that of the mean basaltic  
304 shergottite composition (Nimmo & Tanaka, 2005), and given the K, Th, and K/Th ratio  
305 signatures, it is more likely to be related to mantle composition than chemical weathering  
306 (Taylor et al., 2006) at least at the scales of our observations. Further, mineralogical  
307 observations by Compact Reconnaissance Imaging Spectrometer for Mars (CRISM) reveal  
308 mafic mineral signatures in outcrops, crater ejecta, and central peaks of the craters in SAP  
309 (Pan et al., 2017) resembling Hesperian-aged volcanism (Salvatore et al., 2010). Also, the  
310 non-detection of Al-bearing sulfates (Figure S7b) that would result from low-pH aqueous  
311 alteration (McLennan, 2012) supports an igneous origin for the apparent depletion of Al. The  
312 collective K and Th enrichment and Al-depletion can best be explained by a low degree of  
313 partial melting at high pressure derived from a garnet-rich mantle source for SAP.

314

## 315 **5. Summary and Conclusion**

316           The first consolidated chemical provinces of Mars reveal several geochemical  
317 signatures of broad geologic import. Our findings demonstrate secular chemical trends among  
318 the southern highland provinces A-C may indicate complex processes of an evolving degree  
319 of partial melting within a highly differentiated mantle source. Distinct lithology of the late  
320 Hesperian lowland unit, Province-D, does not follow the secular chemical trends like  
321 highland provinces. This could provide a mechanism for sampling a high-pressure, garnet-  
322 rich source for Province-D. We also find that even older volatile-rich regions preserve  
323 igneous geochemistry, indicating how throughout Mars's geologic history, water-limited  
324 isochemical weathering dominated regionally to decimeter depths scales. Specifically, as a  
325 distinct plateau of early Hesperian-aged highlands, the Lunae Planum region shows  
326 compositional links – and possibly shared provenance - with Province-A, much like Hesperia  
327 Planum, Syrtis Major, and part of Greater Thaumasia. The similarity of Province-C's K/Th  
328 trend with the average crust and enrichment of volatiles (especially S and Cl) supports mostly  
329 regional volcanic materials (e.g., ashfall pyroclastic deposits), especially for the Medusae  
330 Fossae Formation, despite volatiles' enrichment. In contrast to the provinces A-C, Southern  
331 Acidalia Planitia of Province-D in the northern lowlands is lithologically distinct with the  
332 highest abundance of K and Th of the provinces. However, the similarity of K/Th and  
333 depletion of Al relative to the average crust argues against sedimentary signatures of putative  
334 paleo-ocean(s). The northern lowlands may mostly represent the mafic crust of Mars, which  
335 might have originated by a low degree of partial melting at high pressure as suggested by  
336 high abundances of incompatible elements (K, Th) and Al- depletion rather than the  
337 conventional thought that the northern lowlands are highly fractionated. These findings also  
338 demonstrate the overall utility of the integrative multivariate methodology we have

339 developed for martian geochemical data, motivating possible applications to other planetary  
340 bodies (e.g., Mercury, Moon, and Vesta) with comparable datasets.

341

## 342 **Acknowledgment**

343 AR, ABS, and SN were supported by the Indian Space Research Organization, Director PRL,  
344 Head of Planetary Sciences Division, PRL, and Director IIT Gandhinagar. DRH is supported  
345 by the Baylor Office of the Vice Provost of Research Postdoctoral Program. OG's  
346 contribution was supported by the CNES, based on observations with GRS embarked on  
347 Odyssey. SK's participation was supported by NASA MDAP 80NSSC18K1375. The authors  
348 acknowledge anonymous reviewers for providing constructive and thorough reviews of the  
349 manuscript and Andrew Dombard for editorial handling.

350

351 **Data Availability Statement:** Data in support of this work can be found through Mendeley  
352 data (doi: [10.17632/3jd9whd78m.1](https://doi.org/10.17632/3jd9whd78m.1)). Archival GRS-derived chemical maps are from NASA  
353 Planetary Database System (PDS, [https://pds-  
354 geosciences.wustl.edu/missions/odyssey/grs\\_egs.html](https://pds-geosciences.wustl.edu/missions/odyssey/grs_egs.html)). Mars geology map taken from  
355 USGS-310 archive (<https://pubs.usgs.gov/sim/3292/>), and topographic data from MOLA-  
356 HRSC blended DEM data by [Ferguson et al. \(2018\)](#).

357

358

## 359 **Figure Caption**

360 **Figure 1:** Results obtained from multivariate analysis by NHC-PCA **(a)**, HC-PCA **(b)**, and t-  
361 GTC **(c)** methods, overlaid on the Mars Orbiter Laser Altimeter and High-Resolution Stereo  
362 Camera (MOLA-HRSC) data map ([Smith et al., 2001](#)) to delineate the geochemical  
363 provinces. Provinces-2 and -4 do not appear in the t-GTC method **(c)** as they are  
364 compositionally similar to the average crustal composition (**Tables S2 and S3**). **(d)** The  
365 consolidated geochemical provinces on Mars are derived by integrating provinces from three  
366 different multivariate techniques and overlaid onto mapped geology ([Tanaka et al., 2014](#);



367 different colors indicate different geologic units with major units in legend). The white  
368 dashed outline areas delineate our regional (LP, SAP, and MFF) case studies.

369

370 **Figure 2: (a)** The relative areal fractions of secular, transitional, and volcanic units within  
371 each chemical province corresponding to the consolidated geochemical map. The prefix “N”  
372 indicates Noachian, “H” indicates Hesperian, and “A” indicates Amazonian, and suffix “v”  
373 indicates the associated volcanic units (after, [Tanaka et al., 2014](#)). A detailed version of  
374 Figure 2a is given in Figure S2, both as per [Tanaka et al. \(2014\)](#) geology map. **(b)** Modified  
375 box-and-whiskers diagram to compare the distribution of elements for all provinces to the  
376 global geochemistry of the AMC. The top of the upper box represents 75<sup>th</sup> percentile/25<sup>th</sup>  
377 percentile ratio, the bottom of the lower box represents the 25<sup>th</sup>/75<sup>th</sup> percentile ratio, and the  
378 ratio of the medians by the boundary between them. The whiskers here represent the  
379 uncertainty on the ratio of medians using the Median Absolute Deviation (MAD)  
380 ([Karunatillake et al., 2011](#)). **(c)** The Chemical Index of Alteration  
381 ( $CIA=100*[Al_2O_3/(Al_2O_3+CaO+Na_2O+K_2O)]$ ) diagram is used to assess the extent of  
382 chemical weathering in the provinces A-D. For CIA, we are using standard molar abundances  
383 of oxides. Non-GRS Na<sub>2</sub>O is calculated using [Baratoux et al. \(2014\)](#).

384

385 **Figure 3:** Diagrams of K/Th normalized to the bulk silicate Mars (~ 5300) versus GRS  
386 derived total volatile concentration **(a)**, Fe versus Si **(b)**, Al versus Fe **(c)**, and Ca versus Si  
387 **(d)** of the provinces A-D are represented by colored boxes (southern highland provinces A-C)  
388 and ellipse (northern lowland Province-D). The modest variation in K/Th is consistent with  
389 the bulk Mars, implies to low or no alteration at decimeter depths in the consolidated  
390 provinces. The regional uncertainty is shown at the right corner of each plot, represented by

391 the average of standard error of mean ( $1\sigma$ ) from all provinces (**Table 1**). From Noachian to  
392 Amazonian, all the three plots (**b-d**) exhibit a compositional trend, marked by a dashed  
393 arrow, except Province-D (**Figure S2**). The prefix “N” indicates Noachian, “H” indicates  
394 Hesperian, and “A” indicates Amazonian, and the suffix “v” indicates associated volcanic  
395 units, “h” indicates highland, “m” indicates middle and “lHI” indicates late Hesperian  
396 lowland. **(e)** The scatter values of K (wt. %) versus Th (mg/kg) in Southern Acidalia Planitia  
397 (SAP), Lunae Planum (LP), Medusae Fossae Formation (MFF), consolidated provinces A-D,  
398 and AMC. SAP, LP, and MFF generally follow the same trend of K/Th as the AMC.

399

400

401

402

403

404

405

406

407

408

409

410

411

412 **References**

- 413 Balta, J. B., & McSween Jr, H. Y. (2013). Water and the composition of Martian magmas.  
414 *Geology*, *41*, 1115-1118. <https://doi.org/10.1130/G34714.1>.
- 415 Bandfield, J. L., Hamilton, V. E., & Christensen, P. R. (2000). A global view of Martian  
416 surface compositions from MGS-TES: *Science*, *287*, 1626-1630,  
417 <https://doi.org/10.1126/science.287.5458.1626>.
- 418 Baratoux, D., Toplis, M. J., Monnereau, M., & Gasnault, O. (2011). Thermal history of Mars  
419 inferred from orbital geochemistry of volcanic provinces. *Nature*, *472*, 338–341.  
420 <https://doi.org/10.1038/nature09903>
- 421 Baratoux, D., Toplis, M. J., Monnereau, M., & Sautter, V. (2013). The petrological  
422 expression of early Mars volcanism. *Journal of Geophysical Research: Planets*, *118*(1),  
423 59-64. <https://doi.org/10.1029/2012JE004234>
- 424 Baratoux, D., Samuel, H., Michaut, C., Toplis, M. J., Monnereau, M., Wieczorek, M., et al.  
425 (2014). Petrological constraints on the density of the Martian crust. *Journal of*  
426 *Geophysical Research: Planets*. *119*, 1707-1727.  
427 <https://doi.org/10.1002/2014JE004642>
- 428 Basu Sarbadhikari, A., Babu, E. V. S. S. K., Vijaya Kumar, T., & Aoudjehane, H. C. (2016).  
429 Martian meteorite Tissint records unique petrogenesis among the depleted shergottites.  
430 *Meteoritics and Planetary Science*, *51*:1588–1610. <https://doi.org/10.1111/maps.12684>
- 431 Basu Sarbadhikari, A., Babu, E. V. S. S. K., & Vijaya Kumar, T. (2017). Chemical layering  
432 in the upper mantle of Mars: Evidence from olivine-hosted melt inclusions in Tissint.  
433 *Meteoritics and Planetary Science*, *52*, 251-267. <https://doi.org/10.1111/maps.12790>
- 434 Bevington, P. R., & Robinson, D. K. (2003). Data reduction and error analysis. *McGraw-Hill*,

435 New York.

436 Borg, L. E., & D. S. Draper (2003). A petrogenetic model for the origin and compositional  
437 variation of the Martian basaltic meteorites, *Meteoritics & Planetary Science*, 38,  
438 1713–1731. <https://doi.org/10.1111/j.1945-5100.2003.tb00011.x>

439 Bouley, S., Keane, J.T., Baratoux, D., Langlais, B., Matsuyama, I., et al. (2020). A thick  
440 crustal block revealed by reconstructions of early Mars highlands. *Nature Geoscience*.  
441 13, 105–109. <https://doi.org/10.1038/s41561-019-0512-6>

442 Boynton, W. V, Taylor, G. J., Evans, L. G., Reedy, R. C., Starr, R., Janes, D. M., et al.  
443 (2007). Concentration of H, Si, Cl, K, Fe, and Th in the low- and mid-latitude regions  
444 of Mars. *Journal of Geophysical Research: Planets*, 112, 1–15,  
445 <https://doi.org/10.1029/2007JE002887>

446 Charrad M., Ghazzali N., Boiteau V., & Niknafs A. (2014). NbClust: An R Package for  
447 Determining the Relevant Number of Clusters in a Data Set. *Journal of Statistical*  
448 *Software*, 61, 1-36. <http://www.jstatsoft.org/v61/i06/>.

449 Cormack, R. M. (1971). A review of classification. *Journal of the Royal Statistical Society:*  
450 *Series A (General)*, 134, 321-353.

451 Dasgupta, R., & Hirschmann, M.M. (2007). A modified iterative sandwich method for  
452 determination of near-solidus partial melt compositions. II. Application to  
453 determination of near-solidus melt compositions of carbonated peridotite, *Contributions*  
454 *to Mineralogy and Petrology*, 154, 647–661, [https://doi.org/10.1007/s00410-007-0214-](https://doi.org/10.1007/s00410-007-0214-8)  
455 8.

456 Diez, B., Feldman, W. C., Maurice, S., Gasnault, O., Prettyman, T. H., & Mellon, M. T.  
457 (2008). H layering in the top meter of Mars. *Icarus*, 196, 409–421.  
458 <https://doi.org/10.1016/j.icarus.2008.02.006>

459 Diez, B., Feldman, W. C., Mangold, N., Baratoux, D., Maurice, S., Gasnault, O., et al.  
460 (2009). Contribution of Mars Odyssey GRS at central Elysium Planitia. *Icarus*, 2001, 19-  
461 29. <https://doi.org/10.1016/j.icarus.2008.11.011>

462 Ehlmann, B. L., Mustard, J. F., Murchie, S. L., Bibring, J. P., Meunier, A., Fraeman, A. A., &  
463 Langevin, Y. (2011). Subsurface water and clay mineral formation during the early  
464 history of Mars. *Nature*, 479, 53–60. <https://doi.org/10.1038/nature10582>

465 Feldman, W. C., Head, J. W., Maurice, S., Prettyman, T. H., Elphic, R. C., Funsten, H. O., et  
466 al. (2004). Recharge mechanism of near-equatorial hydrogen on Mars: Atmospheric  
467 redistribution or sub-surface aquifer. *Geophysical Research Letters*, 31, 2–5.  
468 <https://doi.org/10.1029/2004GL020661>

469 Feldman, W. C., Pathare, A., Maurice, S., Prettyman, T. H., Lawrence, D. J., Milliken, R. E.,  
470 & Travis, B. J. (2011). Mars Odyssey neutron data: 2. Search for buried excess water  
471 ice deposits at nonpolar latitudes on Mars. *Journal of Geophysical Research: Planets*,  
472 116, E11009. <https://doi.org/10.1029/2011JE003806>

473 Ferguson, R. L., Hare, T. M., & Laura, J. (2018). HRSC and MOLA blended digital elevation  
474 Model at 200m v2. *Astrogeology PDS annex*. U.S. Geological Survey. Retrieved from  
475 [http://bit.ly/HRSC\\_MOLA\\_Blend\\_v0](http://bit.ly/HRSC_MOLA_Blend_v0).

476 Gasnault, O., Taylor, J. G., Karunatillake, S., Dohm, J., Newsom, H., Forni, O., et al. (2010).  
477 Quantitative geochemical mapping of martian elemental provinces. *Icarus*, 207, 226–  
478 247. <https://doi.org/10.1016/j.icarus.2009.11.010>

479 Goetz, W., Bertelsen, P., Binau, C. S., Gunnlaugsson, H. P., Hviid, S. F., Kinch, K. M., et al.  
480 (2005). Indication of drier periods on Mars from the chemistry and mineralogy of  
481 atmospheric dust. *Nature*. 436, 62–65. <https://doi.org/10.1038/nature03807>

- 482 Golombek, M.P., & Phillips, R.J. (2009) Mars tectonics, *Planetary tectonics*. Cambridge  
483 University Press, 11, 180–232.
- 484 Grott, M., Baratoux, D., Hauber, E., Sautter, V., Mustard, J., Gasnault, O., et al. (2013).  
485 Long-term evolution of the Martian crust-mantle system, *Space Science Reviews*,  
486 174(1), 49-111. <https://doi.org/10.1007/s11214-012-9948-3>
- 487 Halevy, I., Zuber, M. T., & Schrag, D. P. (2007). A Sulfur Dioxide Climate Feedback on  
488 Early Mars, *Science*, 318, 1903–1908. <https://doi.org/10.5040/9780755621101.0007>
- 489 Hood, D. R., Judice, T., Karunatillake, S., Rogers, D., Dohm, J. M., Susko, D., & Carnes, L.  
490 K. (2016). Assessing the geologic evolution of Greater Thaumasia, Mars. *Journal of*  
491 *Geophysical Research: Planets*. 121, 1753–1769,  
492 <https://doi.org/10.1002/2016JE005046>
- 493 Hood, D. R., Karunatillake, S., Gasnault, O., Williams, A. J., Dutrow, B., Ojha, L., Kobs, S.,  
494 Kim, K., Heldmann, J., & Fralick, C. (2019). Contrasting regional soil alteration across  
495 the topographic dichotomy of Mars. *Geophysical Research Letters*, 46, 13668-13677.  
496 <https://doi.org/10.1029/2019GL084483>
- 497 Hurowitz, J. A., & McLennan, S. M. (2007). A ~3.5 Ga record of water-limited, acidic  
498 weathering conditions on Mars, *Earth and Planetary Science Letters*, 260 (3–4), 432–  
499 443, <https://doi.org/10.1016/j.epsl.2007.05.043>.
- 500 Karunatillake, S., Squyres, S. W., Taylor, G. J., Keller, J. M., Gasnault, O., Evans, L. G., et  
501 al. (2006). Composition of northern low-albedo regions of Mars: Insights from the  
502 Mars Odyssey Gamma Ray Spectrometer. *Journal of Geophysical Research*, 111.  
503 <https://doi.org/10.1029/2006JE002675>

504 Karunatillake, S., Wray, J. J., Squyres, S. W., Taylor, G. J., Gasnault, O., McLennan, S. M., et  
505 al. (2009). Chemically striking regions on Mars and Stealth revisited, *Journal of*  
506 *Geophysical Research: Planets*, 114, 1–35. <https://doi.org/10.1029/2008JE003303>

507 Karunatillake, S., Squyres, S. W., Gasnault, O., Keller, J. M., Janes, D. M., Boynton, W. V.,  
508 et al. (2011). Recipes for spatial statistics with global datasets: a martian case study.  
509 *Journal of Scientific Computing*, 46, 439-451. [https://doi.org/10.1007/s10915-010-](https://doi.org/10.1007/s10915-010-9412-z)  
510 9412-z

511 Kaufman, L., & Rousseeuw, P.J. (2005). Finding Groups in Data: An Introduction to Cluster  
512 Analysis. *John Wiley & Sons*, New York.

513 Keller, J. M., Boynton, W. V., Karunatillake, S., Baker, V. R., Dohm, J. M., Evans, L. G., et  
514 al. (2006). Equatorial and midlatitude distribution of chlorine measured by Mars  
515 Odyssey GRS. *Journal of Geophysical Research: Planets*, 111, 1–18.  
516 <https://doi.org/10.1029/2006JE002679>

517 Kerber, L., & Head, J. W. (2010). The age of the Medusae Fossae Formation: Evidence of  
518 Hesperian emplacement from crater morphology, stratigraphy, and ancient lava  
519 contacts. *Icarus*, 206 (2), 669–684. <https://doi.org/10.1016/j.icarus.2009.10.001>

520 King, P.L., & McLennan, S.M. (2010). Sulfur on Mars. *Elements* 6, 107-112.

521 Maurice, S., Feldman, W., Diez, B., Gasnault, O., Lawrence, D. J., Pathare, A., & Prettyman,  
522 T. (2011). Mars Odyssey neutron data: 1. Data processing and models of water-  
523 equivalent-hydrogen distribution. *Journal of Geophysical Research: Planets*, 116.  
524 <https://doi.org/10.1029/2011JE003810>

525 McLennan, S. M. (2012). Geochemistry of Sedimentary Processes on Mars, Sedimentary  
526 Geology of Mars. *Sedimentary Geology of Mars*. Special Publication 102, 119–138,  
527 <https://doi.org/10.2110/pec.12.102.0119>

- 528 McSween Jr, H. Y., Taylor, G. J., & Wyatt, M. B. (2009). Elemental Composition of the  
529 Martian Crust. *Science*, 324(5928), 736-739. <https://doi.org/10.1126/science.1165871>
- 530 Newsom, H. E., & Hagerty, J. J. (1997). Chemical components of the Martian soil: Melt  
531 degassing, hydrothermal alteration, and chondritic debris. *Journal of Geophysical*  
532 *Research: Planets*, 102, 19345-19355. <https://doi.org/10.1029/97JE01687>
- 533 Nimmo, F., & Tanaka, K. (2005). Early crustal evolution of Mars. *Annual Review of Earth*  
534 *and Planetary Sciences*, 33, 133–161.  
535 <https://doi.org/10.1146/annurev.earth.33.092203.122637>
- 536 Ojha, L., Lewis, K., Karunatillake, S., & Schmidt, M. (2018). The Medusae Fossae  
537 Formation as the single largest source of dust on Mars. *Nature Communications*, 9, 1–  
538 7. <https://doi.org/10.1038/s41467-018-05291-5>
- 539 Ojha, L., Karunatillake, S., Karimi, S., & Buffo, J. (2021). Amagmatic hydrothermal systems  
540 on Mars from radiogenic heat. *Nature Communications*, 12, 1-11.  
541 <https://doi.org/10.1038/s41467-021-21762-8>
- 542 Pan, L., Ehlmann, B. L., Carter, J., & Ernst, C. M. (2017). The stratigraphy and history of  
543 Mars' northern lowlands through mineralogy of impact craters. A comprehensive  
544 survey. *Journal of Geophysical Research: Planets*, 122, 1824–1854.  
545 <https://doi.org/10.1002/2017JE005276>
- 546 Plesa, A.C., Padovan, S., Tosi, N., Breuer, D., Grott, M., Wiczorek, M. A., et al. (2018). The  
547 thermal state and interior structure of Mars. *Geophysical Research Letters*, 45, 198–12.  
548 <https://doi.org/10.1029/2018GL080728>



549 Rogers, A. D., Bandfield, J. L., & Christensen, P. R. (2007). Global spectral classification of  
550 Martian low-albedo regions with Mars Global Surveyor Thermal Emission  
551 Spectrometer (MGS-TES) data. *112*, 1–29. <https://doi.org/10.1029/2006JE002726>

552 Rogers, A. D., & Hamilton, V. E. (2015). Compositional provinces of Mars from statistical  
553 analyses of TES, GRS, OMEGA and CRISM data. *Journal of Geophysical Research:*  
554 *Planets*, *120*, 62–91. <https://doi.org/10.1002/2014JE004690>

555 Rousseeuw, P.J. (1987). Silhouettes: A graphical aid to the interpretation and validation of  
556 cluster analysis. *Journal of Computational and Applied Mathematics*, *20*, 53–65.

557 Salvatore, M. R., Mustard, J. F., Wyatt, M. B., & Murchie, S. L. (2010). Definitive evidence  
558 of Hesperian basalt in Acidalia and Chryse Planitiae. *Journal of Geophysical Research*,  
559 *115*, E07005. <https://doi.org/10.1029/2009JE003519>

560 Smith, D. E., Zuber, M. T., Frey, H. V., Garvin, J. B., Head, J. W., Muhleman, D. O., et al.  
561 (2001). Mars Orbiter Laser Altimeter: Experiment summary after the first year of  
562 global mapping of Mars. *Journal of Geophysical Research: Planets*, *106*, 23689–23722.  
563 <https://doi.org/10.1029/2000JE001364>

564 Tanaka, K. L., Skinner, J. A., Dohm, J. M., Irwin, R. P., I., Kolb, E. J., Fortezzo, C. M., et al.  
565 (2014). Description of Map Units, p. 1–43, <https://doi.org/10.133/sim3292>

566 Taylor, G. J. (2013). The bulk composition of Mars. *Geochemistry*. *73*, 401–420.  
567 <https://doi.org/10.1016/j.chemer.2013.09.006>

568 Taylor, G. J., Stopar, J. D., Boynton, W. V., Karunatillake, S., Keller, J. M., Brückner, J., et  
569 al. (2006). Variations in K/Th on Mars. *Journal of Geophysical Research*, *112*,  
570 E03S06. <https://doi.org/10.1029/2006JE002676>

571 Taylor, G. J., Martel, L. M. V., Karunatillake, S., Gasnault, O., & Boynton, W. V. (2010).  
572 Mapping Mars geochemically. *Geology*, 38, 183–186.  
573 <https://doi.org/10.1130/G30470.1>

574 Tosca, N. J., McLennan, S. M., Dyar, M. D., Sklute, E. C., & Michel, F. M. (2008). Fe  
575 oxidation processes at Meridiani Planum and implications for secondary Fe mineralogy  
576 on Mars. *Journal of Geophysical Research: Planets*, 113(E5).  
577 <https://doi.org/10.1029/2007JE003019>

578 Treiman, A.H., (2005). The nakhlite meteorites: Augite-rich igneous rocks from Mars:  
579 *Chemie der Erde Geochemistry*, 65, 203–270,  
580 <https://doi.org/10.1016/j.chemer.2005.01.004>.

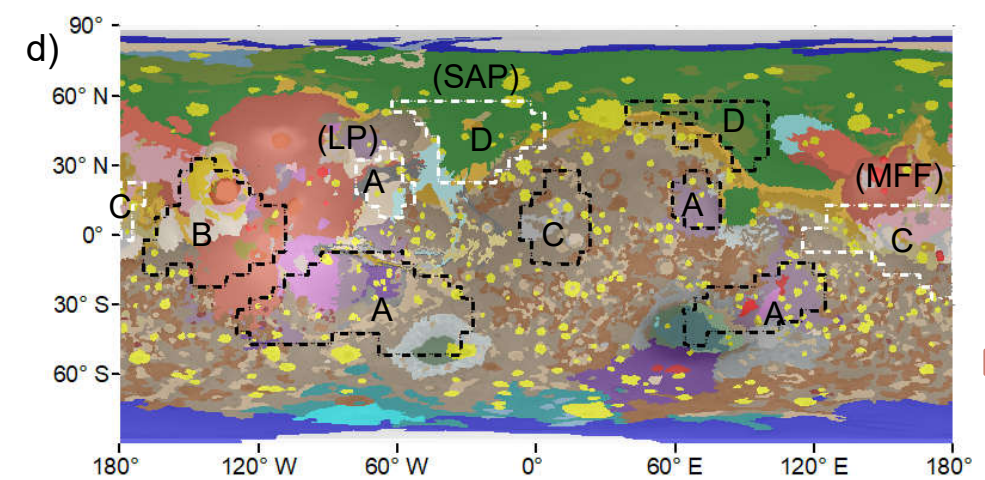
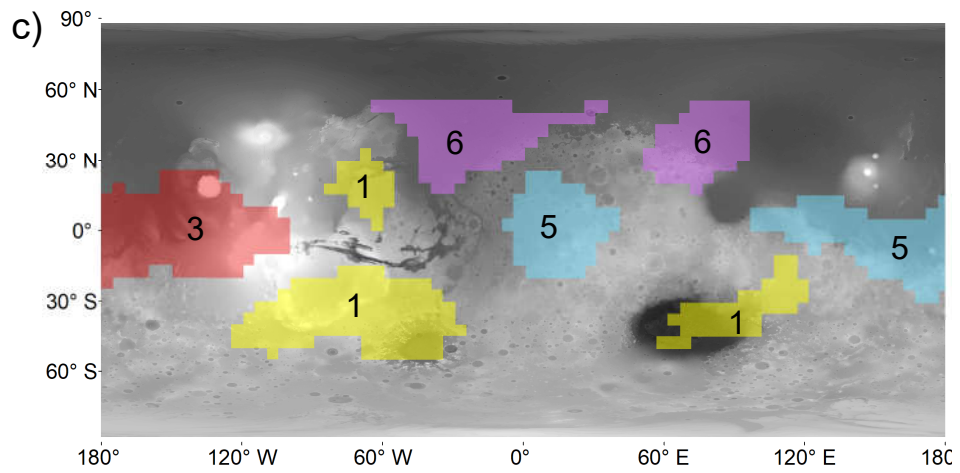
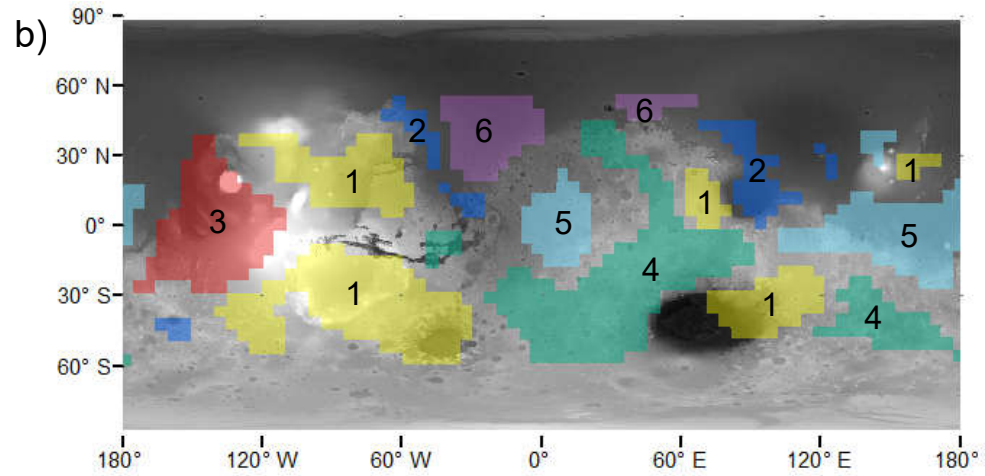
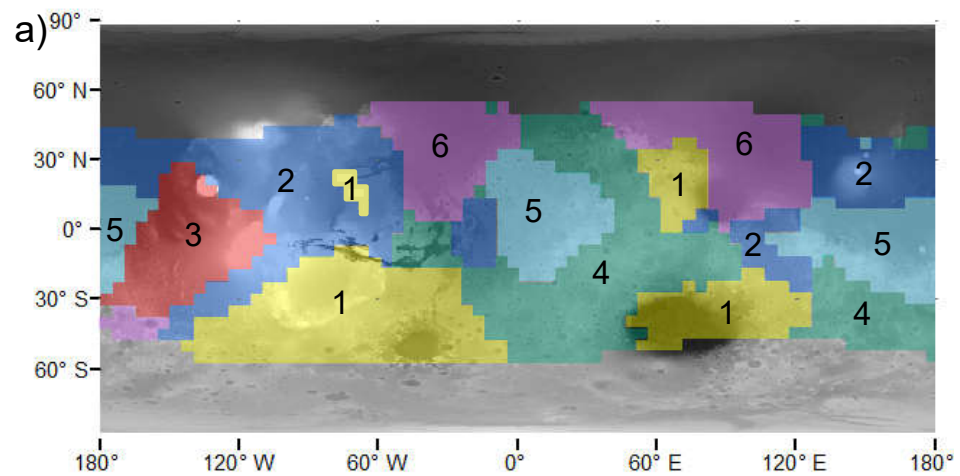
581 Udry, A., Howarth, G. H., Herd, C. D. K., Day, J. M., Lapen, T. J., & Filiberto, J. (2020).  
582 What martian meteorites reveal about the interior and surface of Mars, *Earth Space*  
583 *Science Open Archive* 55, <https://doi.org/10.1002/essoar.10503123.1>.

584 Wilson, J. T., Eke, V. R., Massey, R. J., Elphic, R. C., Feldman, W. C., Maurice, S., &  
585 Teodoro, L. F. A. (2018). Equatorial locations of water on Mars: Improved resolution  
586 maps based on Mars Odyssey Neutron Spectrometer data. *Icarus*, 299, 148–160.  
587 <https://doi.org/10.1016/j.icarus.2017.07.028>

588 Zimbelman, J. R., & Scheidt, S. P. (2012). Hesperian Age for Western Medusae, Mars,  
589 *Science*, 336(6089), 1683-1683. <https://doi.org/10.1126/science.1221094>

590

Figure 1.



Major Geologic units  
after Tanaka et al.  
(2014) for Figure 1d

- Middle Noachian highland
- Early Hesperian volcanic
- Late Hesperian lowland
- Amazonian Hesperian volcanism

Figure 2.

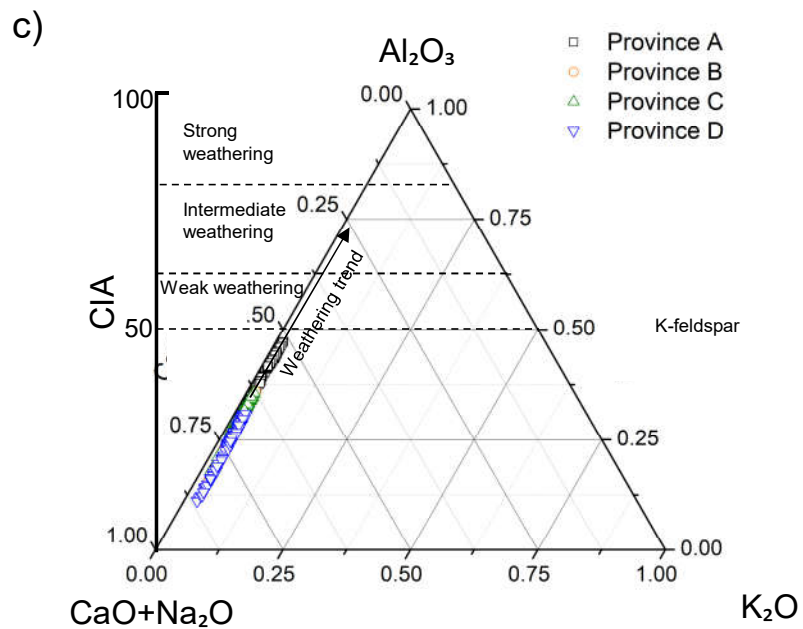
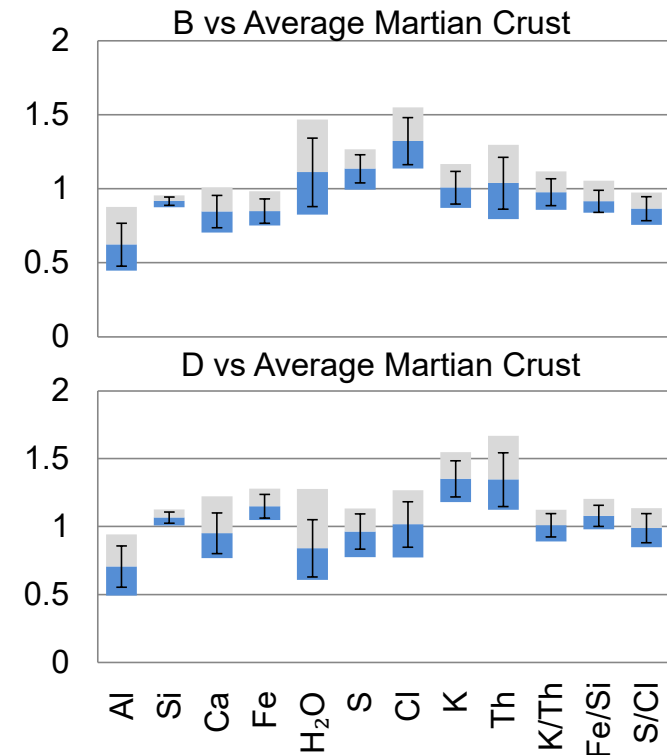
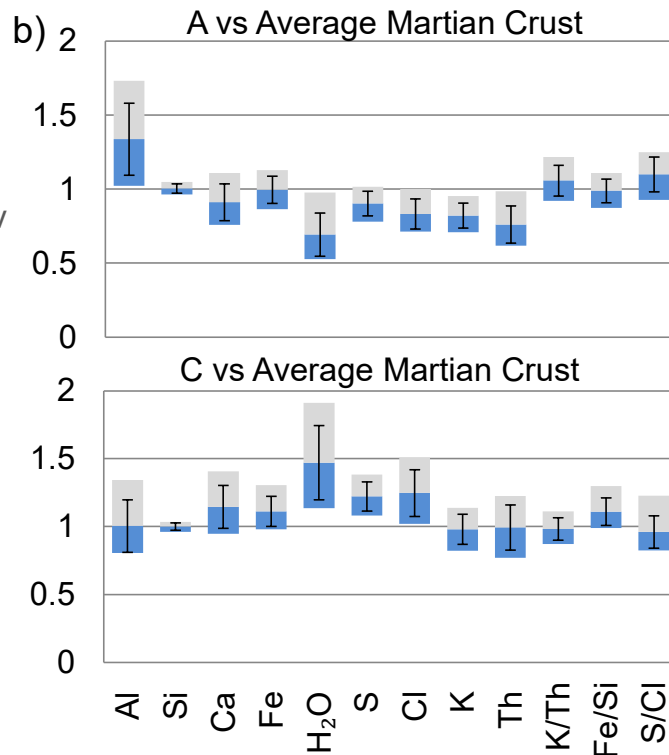
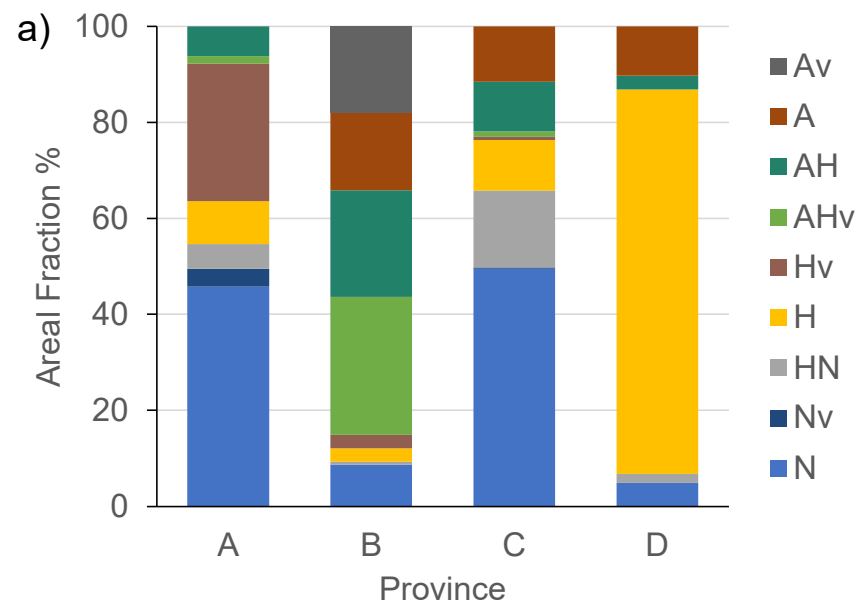
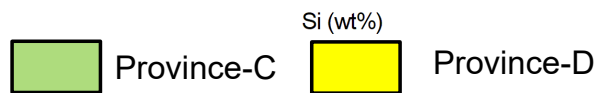
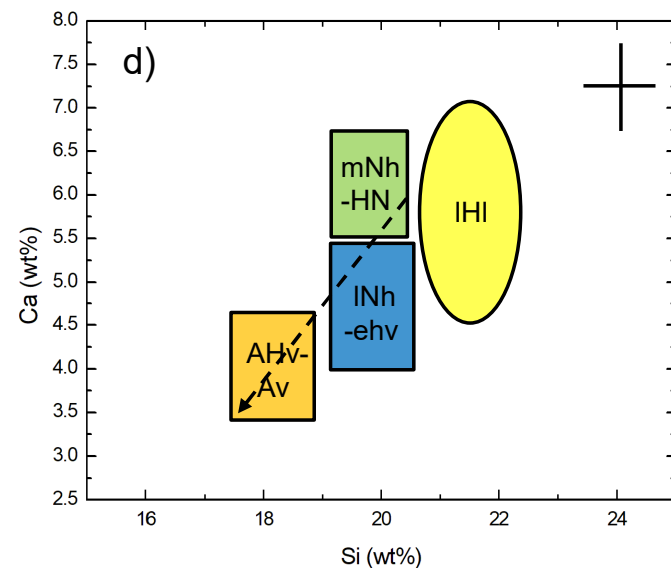
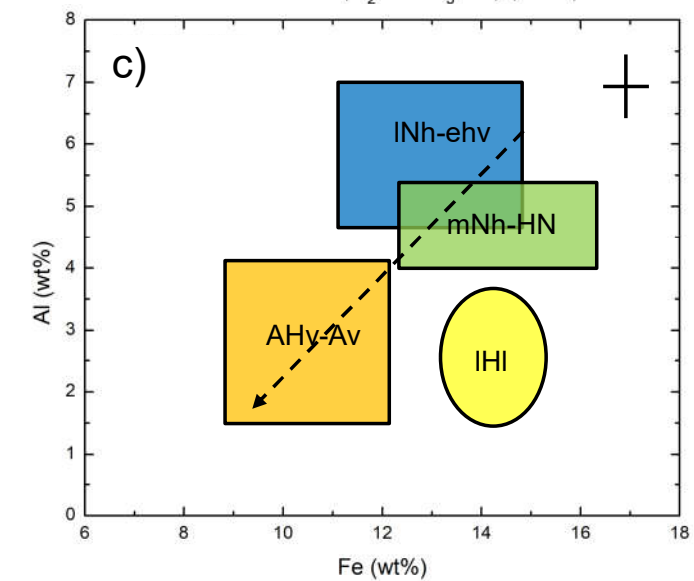
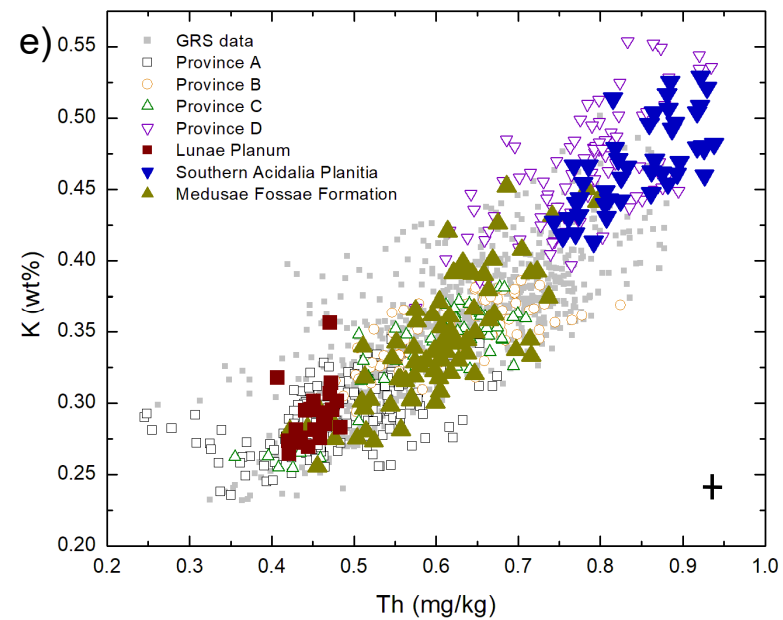
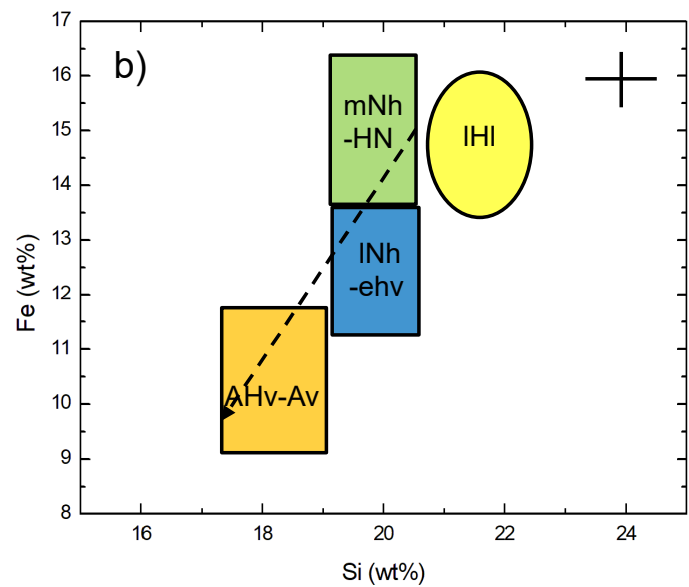
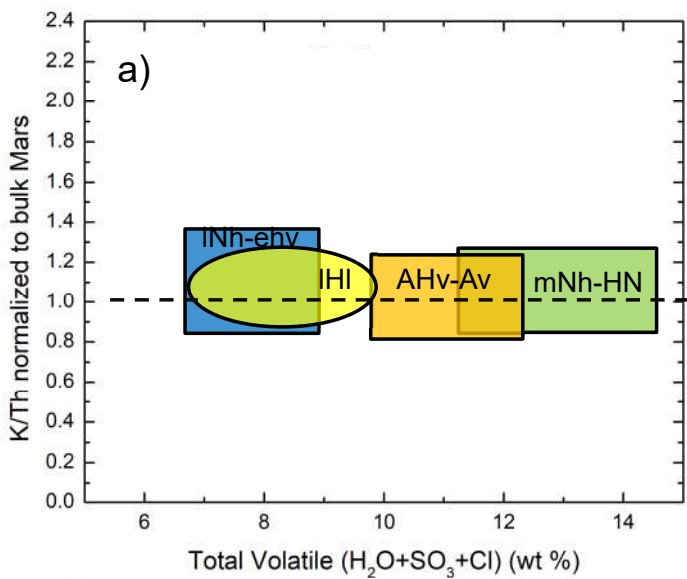


Figure 3.





**Table 1:** Arithmetic mean stoichiometric oxide mass fraction as a percentage (wt%, if not mentioned otherwise), elemental ratio, and its corresponding root means square uncertainty ( $\sigma$ ) are calculated from mean measurement uncertainties for the grid points composing a geochemical province. Whereas, K/Th ratio uncertainty is calculated from  $[(K/Th)*((\sigma_K/K)^2+(\sigma_{Th}/Th)^2)]^{1/2}$  (GRS derived) of the consolidated chemical provinces.

	<b>Province-A</b>	<b>Province-B</b>	<b>Province-C</b>	<b>Province-D</b>	<b>Mid-latitudinal Average Martian Crust (AMC)</b>
<b>K<sub>2</sub>O</b>	0.35±0.01	0.42±0.01	0.40±0.01	0.56±0.02	0.43±0.01
<b>FeO</b>	16.1±0.9	14.0±0.8	18.2±1.1	18.4±1.2	16.3±1.0
<b>SiO<sub>2</sub></b>	42.7±2.3	39.1±2.1	42.4±2.6	44.9±3.0	42.5±2.5
<b>CaO</b>	6.6±1.2	5.9±1.1	7.9±1.4	6.9±1.7	7.0±1.3
<b>Th mg/kg</b>	0.48±0.04	0.62±0.05	0.59±0.05	0.80±0.06	0.61±0.05
<b>Al<sub>2</sub>O<sub>3</sub></b>	10.6±2.1	5.5±1.8	8.6±2.2	6.2±2.6	8.5±2.2
<b>H<sub>2</sub>O</b>	2.9±0.4	4.2±0.4	5.5±0.5	3.5±0.6	3.9±0.5
<b>Cl</b>	0.41±0.03	0.61±0.03	0.57±0.04	0.46±0.04	0.47±0.03
<b>SO<sub>3</sub></b>	4.9±0.5	6.0±0.5	6.5±0.6	5.2±0.7	5.4±0.6
<b>K/Th</b>	6060±580	5600±430	5680±520	5800±440	5760±470